

SINPOINT: A NOVEL TOPOLOGICAL CONSISTENT AUGMENTATION FOR POINT CLOUD UNDERSTANDING

Anonymous authors

Paper under double-blind review

ABSTRACT

Data augmentation is a highly effective method for addressing the issue of data scarcity in machine learning and computer vision tasks. It involves diversifying the original data through a series of transformations to improve the robustness and generalization ability of the model. However, due to the disorder and irregularity of point clouds, existing methods struggle to enrich geometric diversity and maintain topological consistency, leading to imprecise point cloud understanding. In this paper, we propose SinPoint, a novel method designed to preserve the topological structure of the original point cloud through a homeomorphism. Additionally, it utilizes the Sine function to generate smooth displacements. This simulates object deformations, thereby producing a rich diversity of samples. Our extensive experiments demonstrate that SinPoint consistently outperforms existing Mixup and Deformation methods on various benchmark point cloud datasets, improving performance for shape classification and part segmentation tasks. Specifically, when used with PointNet++ and DGCNN, SinPoint achieves a state-of-the-art accuracy of 90.2 on shape classification with the real-world ScanObjectNN dataset. Furthermore, our method is highly versatile and scalable, and it can adapt to different scenarios and requirements for point cloud tasks.

1 INTRODUCTION

With the widespread application of deep learning in computer vision, the point cloud, as a crucial representation of three-dimensional shapes, is gradually attracting attention from the industry Qi et al. (2017a;b); Li et al. (2018); Thomas et al. (2019); Lin et al. (2020a); Qian et al. (2022). Compared to traditional two-dimensional images, point clouds offer richer three-dimensional spatial information, providing broader application prospects for areas such as autonomous driving Navarro-Serment et al. (2010); Kidono et al. (2011); Chen et al. (2017), scene understanding Verdoja et al. (2017); Chen et al. (2019a); Sugimura et al. (2020), and virtual reality Rusu et al. (2008); Qi et al. (2018). However, due to the dual constraints of technology and cost, there are relatively small-scale 3D datasets with limited labels and diversity. This limitation can cause the problem of overfitting and further affect the generalization ability of the network. Facing such challenges, effectively using limited point cloud data for better training deep learning models has been an urgent problem to address. Recently, **Data Augmentation** (DA) has become a popular strategy in avoiding overfitting and improving the generalizability of models by increasing the quantity and diversity of samples.

DA has shown significant success in handling image data. Various methods, such as Cutout DeVries & Taylor (2017); Zhong et al. (2020), Mixup Zhang et al. (2017), Cutmix Yun et al. (2019), and other methods Verma et al. (2019); Yang et al. (2022), have been utilized to augment images and enhance the robustness and generalizability of models. However, unlike regular images, point clouds are disordered and irregular, making it challenging to apply these DA methods directly to point cloud data. Some existing point cloud DA methods only focus on a single type of operation, such as simple geometric transformations (rotation, scaling, and translation), data perturbations (adding noise and deleting points), or hybrid operations (simulated mixtures of images Chen et al. (2020); Lee et al. (2022; 2021); Zhang et al. (2022); Ren et al. (2022); Wang et al. (2024)). While these methods may improve data diversity to some extent, they often overlook the point cloud’s intrinsic structure and semantic details, resulting in a loss of topological consistency in the augmented point cloud. For instance, PointMixup Chen et al. (2020), PointCutMix Zhang et al. (2022), and SageMix Lee et al. (2022) all use different strategies to mix

054 samples, but they do not consider the local structure of each sample. PointAugment Li et al.
 055 (2020) relies on a learnable transformation matrix, making the outcome unpredictable. Simi-
 056 larly, PointWOLF Kim et al. (2021) transforms local point clouds using a combination of strate-
 057 gies, which can lead to data distortion and significant semantic deviation, as shown in Figure 1.
 058

059 In point cloud processing, maintaining topological consistency is crucial for ensuring the accuracy and per-
 060 formance of the model. Studies have shown that frameworks
 061 such as PointNet++ Qi et al. (2017b), DGCNN Wang
 062 et al. (2019b), Point Cloud Transformer Guo et al. (2021),
 063 and PointMLP Ma et al. (2022) can improve the embed-
 064 ded representation of input data by using techniques like
 065 farthest point sampling and k-nearest neighbor search.
 066 These frameworks effectively capture the spatial structure
 067 and contextual information of the point cloud by preserv-
 068 ing the point cloud’s topological relationships. Further
 069 investigation Lee et al. (2022) has revealed that when the
 070 topology of the point cloud is destroyed, the model can-
 071 not learn the correct representation, leading to decreased
 072 performance. Therefore, in point cloud augmentation, it
 073 is vital to maintain topological consistency while increas-
 074 ing the geometric diversity of samples. However, unlike
 075 topological consistency, which emphasizes keeping the
 076 connections between points unchanged, geometric diversi-
 077 ty usually refers to the augmented point cloud having a
 078 wider range of shapes, sizes, and spatial
 079 distributions than the original point cloud. In other words, geometric diversity is the representation,
 080 while topological consistency is the essence. These two requirements can help ensure the validity
 and reliability of the augmented point cloud.

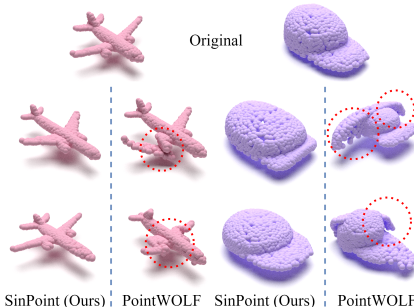


Figure 1: SinPoint ensures a smooth and natural deformation process, avoiding abrupt or unnatural changes. PointWOLF can lead to data distortion and significant semantic deviation.

081 This paper proposes a novel SinPoint transformation technique based on a homeomorphism Derrick
 082 (1973) to address these issues mentioned above. SinPoint aims to preserve the topological structure
 083 of the original point cloud by a homeomorphism Derrick (1973) and perturb the local structure
 084 using a Sine function to simulate the deformation of objects, thereby expanding the diversity of
 085 point clouds. We design two deformation strategies, as shown in Figure 2. One is to use a Single
 086 Sine Function (SinPoint-SSF) with the initial phase as the origin to deform the point cloud. The
 087 other is to use Multiple Sine Function (SinPoint-MSF), with different anchor points as the initial
 088 phase. The sine transforms of different parameters are superimposed to obtain richer deformations.
 089 We experimentally demonstrate that SinPoint outperforms the State-Of-The-Art (SOTA) point cloud
 090 augmentation method on multiple datasets.

091 In summary, our contribution has three main aspects: 1) We propose a novel method for point cloud
 092 DA from the viewpoint of topological consistency and geometric diversity. To the best of our knowl-
 093 edge, this is the first work that incorporates a homeomorphism and Sine function in point cloud DA.
 094 2) We prove that the proposed Sine-based mapping function is a homeomorphism. This can make the
 095 local region of the point cloud produce deformed shapes without destroying the topology, thereby
 096 enhancing the diversity of the point cloud. 3) We demonstrate the effectiveness of our framework
 097 by showing consistent improvements over state-of-the-art augmentation methods on both synthetic
 098 and real-world datasets in 3D shape classification and part segmentation tasks. Our extensive exper-
 099 iments show that SinPoint improves the generalization and robustness of various models.

100
 101 **2 RELATED WORK**

102
 103 **Deep learning on point cloud.** PointNet Qi et al. (2017a) is a pioneering work that uses shared
 104 MLPs to encode each point individually and aggregates all point features through global pooling.
 105 Inspired by CNNs, PointNet++ Qi et al. (2017b) adopts a hierarchical multi-scale or weighted fea-
 106 ture aggregation scheme to get local features. DGCNN Wang et al. (2019b) introduces EdgeConv,
 107 which utilizes edge features from the dynamically updated graph. Additionally, various works have
 focused on point-wise multi-layer perceptron Liu et al. (2020); Xu et al. (2021c); Shen et al. (2018);

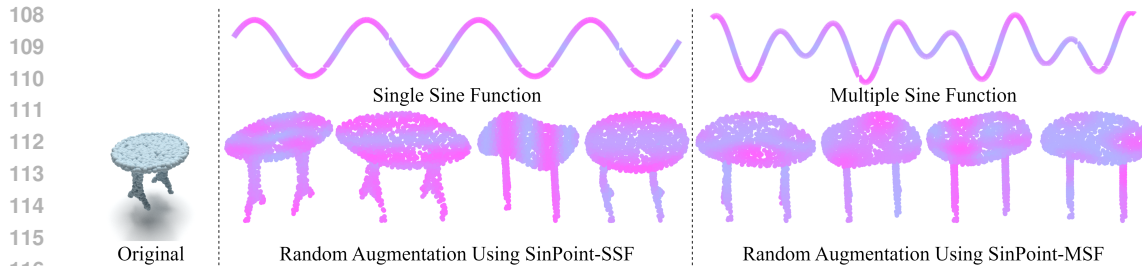


Figure 2: Some augmented samples produced by SinPoint-SSF (left) and SinPoint-MSF (right). The color is close to pink, the deformation is more significant. The data generated by the SinPoint-SSF object has only a single peak, while the samples from SinPoint-MSF have multiple distinct peaks.

Ma et al. (2022); Qian et al. (2022); Zhang et al. (2023), convolution Li et al. (2018); Wu et al. (2019); Thomas et al. (2019); Lin et al. (2020a); Xu et al. (2021b); Liu et al. (2019), and graph-based Qi et al. (2017c); Simonovsky & Komodakis (2017); Wang et al. (2019a); Lin et al. (2020b; 2021) methods to process point clouds. These methods consistently use Conventional Data Augmentation (CDA) Qi et al. (2017a;b); Wang et al. (2019b) to improve the model’s robust kernel generalization performance, but the improvement is relatively marginal. Parallel to these approaches, other recent works Chen et al. (2020); Li et al. (2020); Lee et al. (2022; 2021); Zhang et al. (2022); Kim et al. (2021); Ren et al. (2022); Hong et al. (2023) focus on data augmentation to improve the generalization power of deep neural networks in point clouds.

Data augmentation on point cloud. Current point cloud augmentation methods can be divided into two categories: self-augmentation and mix-augmentation. Self-augmentation through geometric transformation to augment the shape diversity of the point cloud. For instance, CDA Qi et al. (2017a;b); Wang et al. (2019b) encompasses geometric transformations like rotation, scaling, translation, and jittering, alongside the addition of noise and point reduction to enhance sample diversity. PointAugment Li et al. (2020) learn the transformation matrix with an augmentor network to produce augmentations. PointWOLF Kim et al. (2021) selects various anchor points to serve as central points for the local point cloud’s weighted transformation, leading to smooth and varied non-rigid deformations. Mix-augmentation uses different strategies to cut and combine two point clouds to form a new point cloud that contains two local shapes. For example, PointMixup Chen et al. (2020) recently used the shortest path linear interpolation between instances to augment data in the point cloud. PointCutMix Zhang et al. (2022) benefits from CutMixup and PointMixup, and proposes cutting and pasting of point cloud parts. SageMix Lee et al. (2022) proposes a saliency-guided Mixup for point clouds to preserve salient local structures.

3 METHOD

3.1 PRELIMINARIES

Homeomorphism Derrick (1973) is an important mathematical tool used to describe the equivalence relations between topological spaces. It keeps the proximity of points in space unchanged and makes topological Spaces have the same topological properties. These properties make a homeomorphism widely used in topology, geometry, physics, and other fields.

Definition 1. (Homeomorphism) Given two topological spaces X, Y , and given a mapping $f : X \rightarrow Y$. f is a homeomorphism of two spaces when it is satisfied that f is a bijection and f and f^{-1} are continuous, denoted as $X \cong Y$.

Definition 2. (Local homeomorphism) Let $f : X \rightarrow Y$ is a mapping between two topological spaces X and Y . If for every point x in X , exists a neighborhood U of x such that $f(U)$ is an open set in X and $f_U : U \rightarrow f(U)$ is a homeomorphism, then f is a local homeomorphism.

They have similar mathematical properties, both of which require the mapping and its inverse mapping to be continuous and maintain the topological structure of the space Armstrong (2013).

Proposition 1. (Topological consistency) If f is a homeomorphism from X to Y , then X and Y have the same topological properties.

Proposition 2. (Reflexivity, symmetry, and transitivity) The homeomorphic relation is an equivalence relation, and therefore it has reflexivity (any topological space is a homeomorphism to itself), symmetry (if $X \cong Y$, then $Y \cong X$), and transitivity (if $Y \cong Z$, then $X \cong Z$).

Homeomorphism plays a vital role in ensuring topological consistency. First, a homeomorphism is not only one-to-one (bijective) and continuous, but its inverse is also continuous. This guarantees the preservation of the space topology. Second, when processing point clouds, using a homeomorphism can ensure that the basic shape and structure of the point cloud remain unaltered after enhancement or transformation, thus making the augmented data more consistent with the actual scene or object.

3.2 RESIDUAL FUNCTION

Inspired by the deep residual network He et al. (2016), we focus on obtaining continuous residual coordinates and generating augmented coordinates by adding offsets to the original coordinates. Specifically, for a given point cloud $P = \{p_1, p_2, \dots, p_n\}$, we only need to compute the residual coordinates, represented by $P' - P$, thus the augmentation process becomes:

$$P' = P + g(P). \quad (1)$$

A homeomorphism can ensure that the original space and the deformed space have topological consistency. Therefore, it is very important to select the appropriate residual function, which not only gains diversity but also needs to guarantee that the whole mapping is homeomorphic.

3.3 SINPOINT

To simulate the distortion and deformation of an object, we have chosen to use the Sine function as our residual function. The inherent periodic nature of the Sine function allows us to adjust the number of regions that are deformed with precision. Additionally, by manipulating the amplitude of the Sine function, we can precisely control the intensity of the deformation. This displacement field, generated by the Sine function, effectively distorts and deforms specific local regions of the point cloud data without altering the overall topology. As a result, the augmented point cloud data contains more intricate and detailed local features. The standard Sine function is shown below:

$$g(x) = A \sin(\omega x + \varphi), \quad (2)$$

where A , ω , and φ represent the amplitude, the angular velocity (control period), and the initial phase, respectively. The displacement field generated by Sine function is introduced into a homeomorphism, and a homeomorphism based on Sine function can be obtained.

Theorem 1. (Homeomorphism Based on Sine Function) Given two topological spaces X, Y , and given a mapping $f : X \rightarrow Y = X + A \sin(\omega X + \varphi)$, if $-1 \leq A\omega \leq 1$, then f is a homeomorphism, else f is a local homeomorphism. **(The proof is in the Appendix.)**

Since f is a homeomorphism, we can use it to augment the point cloud and ensure its topological consistency. Given a set of points $P = \{p_1, p_2, \dots, p_n\}$, where N represents the number of points in the Euclidean space (x, y, z) . SinPoint applies a homeomorphism and the resulting augmented point cloud P' is given as follows:

$$P' = P + A \sin(\omega P + \varphi), \quad (3)$$

where $A \sin(\omega P + \varphi)$ is displacement field of P . We need to adjust A and ω to produce more diverse point clouds. In this paper, we set $A \sim U(-a, a)$ and $\omega \sim U(-w, w)$ to obey the uniform distribution. In this way, more samples with smooth deformation can be generated, which makes the distribution of samples more uniform.

As illustrated in Figure 3, the transformation of the circle by Equation (3) results in continuous local indentations on the point cloud surface, attributable to the Sine function’s periodic nature. This deformation technique enables the simulation of a concavity similar to that observed when an object is indented while preserving the point cloud’s topology structure.

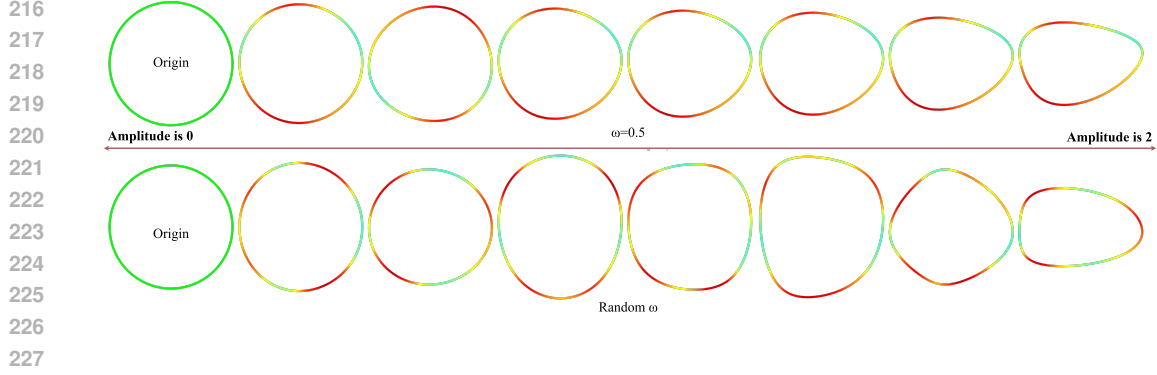


Figure 3: SinPoint obtains different degrees of geometric deformation by controlling the amplitude and angular velocity ω . In the above, only two peaks or troughs appear due to the fixed angular velocity ω . In the following, multiple peaks or troughs occur due to the random angular velocity ω . The darker the color, the larger the deformation.

We designed two transformation strategies for SinPoint, SinPoint-SSF based on a single sine function and SinPoint-MSF based on the superposition of multiple sine functions. Algorithm 1 is the process of generating enhanced samples. Different strategies generate various deformation samples. The two detailed strategies are as follows:

Algorithm 1 SinPoint

Input: Original point cloud $P = \{p_1, p_2, \dots, p_n\}$
Condition *key* for SinPoint-SSF or SinPoint-MSF
Anchor points number k , Amplitude a , Angular velocity ω

Output: P'

- 1: **if** *key* == "SSF"
- 2: Sample $A \sim U(-a, a)$
- 3: Sample $\omega \sim U(-w, w)$
- 4: $P' \leftarrow P + A \sin(\omega P)$
- 5: **else if** *key* == "MSF"
- 6: **if** using farthest point sampling
- 7: $P_i \leftarrow FPS(P, k)$, #FPS() is farthest point sampling
- 8: **else if** using random point sampling
- 9: $P_i \leftarrow RPS(P, k)$, #RPS() is random point sampling
- 10: **end if**
- 11: Sample $A_i \sim U(-a, a), i = 1 : k$
- 12: Sample $\omega_i \sim U(-w, w), i = 1 : k$
- 13: $P' \leftarrow P + \frac{1}{k} \sum_{i=1}^k \{A_i \sin(\omega_i P + P_i)\}$
- 14: **end if**
- 15: **Return** P'

SinPoint-SSF uses a single sine function to perturb the coordinates of the point cloud. We normalize the point cloud to the unit sphere space and take the sphere's center as the initial phase, that is, $\varphi = 0$. Then the SinPoint-SSF transformed point cloud can be expressed as follows:

$$P' = P + A \sin(\omega P). \quad (4)$$

SinPoint-MSF superposes multiple sine functions to perturb the point cloud. Multiple sinusoidal complex waves exhibit rich waveform characteristics through diverse combinations of frequency, amplitude and phase. SinPoint-MSF first selects k anchor points as the initial phase and samples different amplitudes and angular velocities for additive perturbations. This provides more diversity to the point cloud and generates realistic samples. The transformation of SinPoint-MSF as follows:

$$P' = P + \frac{1}{k} \sum_{i=1}^k \{A_i \sin(\omega_i P + \varphi_i)\}, \varphi_i = P_i. \quad (5)$$

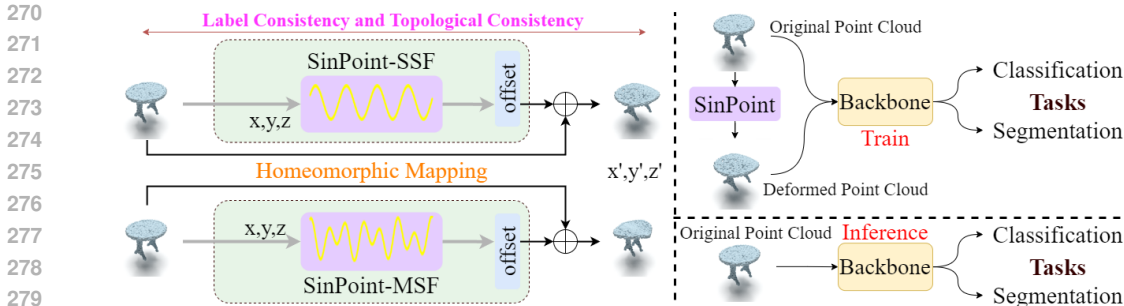


Figure 4: An overview of our SinPoint framework. We use SinPoint to get the augmented point cloud and input it into the network with the original point cloud for training. SinPoint can be adapted for a variety of tasks due to label consistency and topological consistency.

Our framework is shown in Figure 4. It maps the point cloud input to a feature space with topological consistency. By incorporating augmented inputs generated by SinPoint, the training process optimizes the backbone’s parameters in a larger feature space than the baseline. During the training stage, by utilizing the same loss function as the baseline and optimizing in this new augmented feature space, our method learns a more expressive representation that better fits the input data, leading to improved generalization. During inference, the model uses the original point cloud input to preserve the data’s geometric structure, ensuring no disruption to geometric priors in practical applications. Our method maintains point cloud geometric and topological properties. It also extracts more discriminative features, significantly enhancing overall model performance. Our method has been validated on object point clouds.

4 EXPERIMENTS

In this section, we demonstrate the effectiveness of our proposed method, SinPoint, with various benchmark datasets and baselines. First, for 3D shape classification, we evaluate the generalization performance and robustness using SinPoint-SSF in Section 4.1. Next, we compare our SinPoint-MSF with existing data augmentation methods in Section 4.2 for part segmentation. More ablation studies and implementation details are provided in **Appendix**.

Datasets. For classification task, we use two **synthetic datasets**: ModelNet40 (**MN40**) Wu et al. (2015) and Reduced MN40 (**RMN40**), and two **real-world datasets** from ScanObjectNN Uy et al. (2019): **OBJ_ONLY** and **PB_T50_RS**. MN40 is a widely used synthetic benchmark dataset containing 9840 CAD models in the training set and 2468 CAD models in the validation set, with a total 40 classes of common object categories. RMN40 comes from PointMixup Chen et al. (2020) and only contains 20% training samples to simulate data scarcity. ScanObjectNN is a real-world dataset that is split into 80% for training and 20% for evaluation. Among the variants of ScanObjectNN, we adopt the simplest version (**OBJ_ONLY**) and the most challenging version (**PB_T50_RS**). **OBJ_ONLY**, which has 2,309 and 581 scanned objects for the training and validation sets, respectively, and **PB_T50_RS**, which is a perturbed version with 11,416 and 2,882 scanned objects for the training and validation sets, respectively. Both have 15 classes. We use only coordinates (x, y, z) of 1024 points for training models without additional information, such as the normal vector. For the part segmentation task, we adopt a synthetic dataset, **ShapeNetPart** Yi et al. (2016), which contains 14,007 and 2,874 samples for training and validation sets. ShapeNetPart consists of 16 classes with 50 part labels. Each class has 2 to 6 parts.

Baselines. For comparison with previous studies, we use three backbone models: PointNet Qi et al. (2017a), PointNet++ Qi et al. (2017b), and DGCNN Wang et al. (2019b). We compare SinPoint with the model under default augmentation in Base Qi et al. (2017a;b); Wang et al. (2019b) and eight SOTA methods. We report the performance in terms of overall accuracy. To further verify the effectiveness of SinPoint, we add a variety of backbone networks, including RSCNN Liu et al. (2019), PointConv Wu et al. (2019), PointCNN Li et al. (2018), GDANet Xu et al. (2021c), PCT Guo et al. (2021) and PointMLP Ma et al. (2022).

324
325
326
327
328
329
330
331
332
333
334
335
336
337
338
339
340
341
342
343
344
345
346
347
348
349
350
351
352
353
354
355
356
357
358
359
360
361
362
363
364
365
366
367
368
369
370
371
372
373
374
375
376
377

Table 1: 3D shape classification performance on ModelNet40 /ScanObjectNN

Model	Method	ModelNet40		ScanObjectNN	
		MN40	ReducedMN40	OBJ_ONLY	PB_T50_RS
PointNet	Base	89.2	81.9	76.1	64.1
	+PointMixup	89.9	83.4	-	-
	+RSMix	88.7	-	-	-
	+SageMix	90.3	-	79.5	66.1
	+PointCutMix	90.5	-	-	-
	+PointAugment	90.9	84.1	74.4	57.0
	+PatchAugment	90.9	-	-	-
	+PointWOLF	91.1	85.7	78.7	67.1
	+WOLFMix	90.7	-	-	-
	+PCSalMix	90.5	-	-	-
	+PointPatchMix	90.1	-	-	-
+SinPoint(Ours)	91.3 (↑ 2.1)	86.5 (↑ 4.6)	82.6 (↑ 6.5)	70.8 (↑ 6.7)	
PointNet++	Base	90.7	85.9	84.3	79.4
	+PointMixup	92.3	88.6	88.5	80.6
	+RSMix	91.6	-	-	-
	+SageMix	93.3	-	88.7	83.7
	+PointCutMix	93.4	-	-	-
	+PointAugment	92.9	87.0	85.4	77.9
	+PatchAugment	92.4	-	87.1	81.0
	+PointWOLF	93.2	88.7	89.7	84.1
	+WOLFMix	93.1	-	-	-
	+PCSalMix	93.1	-	-	-
	+PointPatchMix	92.9	-	-	-
+SinPoint(Ours)	93.4 (↑ 2.7)	89.6 (↑ 3.7)	90.2 (↑ 5.9)	84.5 (↑ 5.1)	
DGCNN	Base	92.2	87.5	86.2	77.3
	+PointMixup	92.9	89.0	-	-
	+RSMix	93.5	-	-	-
	+SageMix	93.6	-	88.0	83.6
	+PointCutMix	93.2	-	-	-
	+PointAugment	93.4	88.3	83.1	76.8
	+PatchAugment	93.1	-	86.9	79.1
	+PointWOLF	93.2	89.3	88.8	81.6
	+WOLFMix	93.2	-	-	-
	+PCSalMix	93.2	-	-	-
	+SinPoint(Ours)	93.7 (↑ 1.5)	90.1 (↑ 2.6)	90.2 (↑ 4.0)	84.6 (↑ 7.3)

Table 2: 3D shape classification performance in various architectures on ModelNet40.

Model Param.	PointNet	PointNet++	DGCNN	RSCNN	PointConv	PointCNN	GDANet	PCT	PointMLP
	-	1.4M	1.8M	-	18.6M	-	-	2.8M	12.6M
Base	89.2	90.7	92.2	91.7	92.5	92.5	93.4	93.2	94.1
+SinPoint	91.3 (↑ 2.1)	93.4 (↑ 2.7)	93.7 (↑ 1.5)	92.9 (↑ 1.2)	92.8 (↑ 0.3)	93.2 (↑ 0.7)	93.6 (↑ 0.2)	93.5 (↑ 0.3)	94.3 (↑ 0.2)

4.1 3D SHAPE CLASSIFICATION

Comparisons with SOTA Methods. Experimental results of 3D shape classification are shown in Table 1. We report the Overall Accuracy (OA) of each model on all four datasets. From the results, we can clearly see that our SinPoint significantly outperforms all of the previous methods in every dataset and model. Particularly, the average OA improvement on the synthetic datasets is **2.6%**, and the average OA improvement on the real-world datasets is even **5.9%**, and the maximum improvement was DGCNN reaching **7.3%** in PB_T50_RS. It proves that our SinPoint is more efficient on real data sets. These consistent improvements demonstrate the effectiveness of our framework.

3D shape classification performance under Various Network Backbones. The effectiveness of SinPoint is further validated across a variety of network architectures in ModelNet40 Wu et al. (2015) and ScanObjectNN Uy et al. (2019), including PointNet Qi et al. (2017a), PointNet++ Qi

et al. (2017b), DGCNN Wang et al. (2019b), RSCNN Liu et al. (2019), PointConv Wu et al. (2019), PointCNN Li et al. (2018), GDANet Xu et al. (2021c), PCT Guo et al. (2021) and PointMLP Ma et al. (2022), PointNeXt-S Qian et al. (2022), PointMetaBase-S Lin et al. (2023), SPoTr Park et al. (2023). From Table 2, we observe that SinPoint has a consistent improvement of accuracy against the baselines (+0.2~2.7%). Notably, using the basic PointNet++ and DGCNN, we can surpass the Transformer-based baseline PCT while reducing the parameters by half. This reduction compensates for the parameter deficiency in the network through data augmentation alone. Surprisingly, DGCNN+SinPoint is only 0.4% lower than PointMLP, but the parameters are 7 times lower. Table 3 compares some of the latest backbone networks.

Table 3: 3D shape classification performance in various architectures on PB_T50_RS

Model	PointMLP ICLR 2022	PointNeXt-S NeurIPS 2022	PointMetaBase-S CVPR 2023	SPoTr CVPR 2023
Base	85.7	87.7	88.2	88.6
+SinPoint(Ours)	87.5(+1.8)	88.9(+1.2)	89.3(+1.1)	89.5(+0.9)

Table 4: Robustness with DGCNN Wang et al. (2019b) on OBJ_ONLY Uy et al. (2019)

Method	Gaussian noise		Rotation 180°		Scaling		Dropout	
	$\sigma:0.01$	$\sigma:0.05$	X-axis	Z-axis	$\times 0.6$	$\times 2.0$	25%	50%
DGCNN	84.9	48.4	32.5	32.4	73.7	73.0	83.3	75.7
+ PointMixup	85.0	61.3	31.7	32.7	73.8	73.0	84.2	74.9
+ RSMix	84.2	49.1	32.7	32.6	75.0	74.5	84.0	73.6
+ SageMix	85.7	51.2	36.5	37.9	75.6	75.2	84.9	79.0
+ SinPoint	85.9	61.5	38.6	44.1	76.1	75.6	85.1	79.5

Robustness. Additional studies demonstrate our SinPoint improves the robustness of models against previous methods Chen et al. (2020); Lee et al. (2021; 2022) on four types of corruption: (1) **Gaussian noise** with ($\sigma \in (0.01, 0.05)$), (2) **Rotation** 180° (X-axis,Z-axis), (3) **Scaling** with a factor in 0.6, 2.0, and (4) **Dropout** with a rate $r \in \{0.25, 0.50\}$. We adopt DGCNN and OBJ_ONLY to evaluate the robustness of models. As shown in Table 4, SinPoint consistently improves robustness in various corruptions. DGCNN with SinPoint shows the best robustness with significant gains compared to previous methods. Importantly, the gain over the baseline significantly increases as the amount of corruption increases: 13.1% for Gaussian noise ($\sigma : 0.05$), 11.7% for Rotation 180° (Z-axis), 2.6% for Scaling in 2.0, and 3.8% for Dropout ($r = 0.5$). We believe that the diverse samples augmented by a homeomorphism in SinPoint help models to learn more robust features against both ‘local’ and ‘global’ corruptions.

Table 5: Ablation study of SinPoint on ModelNet40 Wu et al. (2015). Mix: mixed training samples.

DGCNN	CDA	Drop	SinPoint(Ours)	Mix(Ours)	OA	Inc.↑
A					91.7	-
B	✓				92.2	0.5
C	✓	✓			92.7	1.0
D			✓		92.9	1.2
E			✓	✓	93.2	1.5
F	✓		✓	✓	93.4	1.7
G	✓	✓	✓	✓	93.7	2.0

Ablation study of modules. Table 5 summarizes the results of the ablation study on DGCNN. Model A gives a baseline classification accuracy of 91.7%. On top of Model A, we use a combination of different augmentors. From the results shown in Table 5, we can see that each augmentation function contributes to producing more effective augmented samples. It is worth noting that when only SinPoint is used, the results already surpass A, B, and C, while using a mixture of original and augmented samples can again improve the generalization performance of DGCNN. Moreover, when

using more modules, the model’s generalization ability is further improved to 93.7%, an improvement of 2.0% over the vanilla.

4.2 3D SHAPE PART SEGMENTATION

SinPoint can also be generalized to other 3D point cloud tasks due to its geometric consistency and label consistency. We first construct SinPoint-SSF and SinPoint-MSF following the optimal parameter settings in the classification task. Next, we test SinPoint for 3D shape part segmentation task on the ShapeNetPart Yi et al. (2016) benchmark. We follow the settings from PointNet, PointNet++ and DGCNN that randomly select 2048 points as input for a fair comparison. We compare our methods with several recent methods, including PointMixup Chen et al. (2020), RSMix Lee et al. (2021), SageMix Lee et al. (2022) and PointWOLF Kim et al. (2021). Table 7 shows that on ShapeNetPart, SinPoint-MSF consistently improves mean IoU (mIoU) over baselines (0.9% over PointNet, 1.0% over PointNet++ and 0.7% over DGCNN), demonstrating the applicability of SinPoint-MSF to point-wise tasks. Notably, SinPoint-MSF has optimal performance in most shapes. It also proves that SinPoint-MSF with more local deformations is effective in part segmentation. Furthermore, Table 6 presents comparative results with state-of-the-art methods, and in the **Appendix**, we offer comparisons against a variety baseline models, where our SinPoint consistently outperforms others. Finally, in Figure 5, we present the visualization results for Sinpoint and baseline.

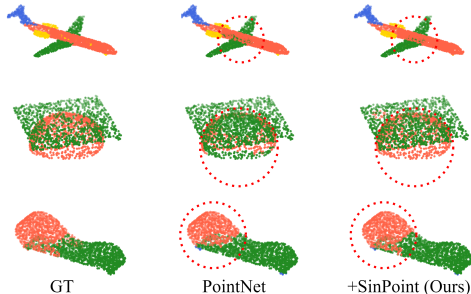


Figure 5: 3D part segmentation experiment visualization results.

Table 6: Overall mean Inter-over-Union (mIoU) on ShapeNetPart Yi et al. (2016).

Method	mIoU	aero	bag	cap	car	chair	aer	guitar	knife	lamp	laptop	motor	mug	pistol	rocket	skate	table
PointNet	83.5	81.8	74.7	80.2	71.9	89.6	71.5	90.3	84.9	79.5	95.2	65.2	91.1	81.1	55.1	72.8	82.2
+PointWOLF	83.8	82.5	73.3	78.8	73.2	89.6	72.2	91.2	86.2	79.7	95.2	64.6	92.5	80.2	56.6	73.1	82.2
+SinPoint-SSF	84.3	82.6	79.8	80.5	77.9	89.4	70.2	91.4	86.6	79.2	95.6	67.6	93.9	82.7	54.6	80.5	82.7
+SinPoint-MSF	84.4	82.4	81.0	84.1	77.3	89.6	70.1	91.4	86.9	79.4	95.6	67.6	93.6	82.9	54.5	81.5	82.8
PointNet++	84.8	81.9	83.4	86.4	78.6	90.5	64.7	91.4	83.1	83.4	95.1	69.6	94.7	82.8	56.9	76.0	82.3
+PointWOLF	85.2	82.0	83.9	87.3	77.6	90.6	78.4	91.1	87.6	84.7	95.2	62.0	94.5	81.3	62.5	75.7	83.2
+SinPoint-SSF	85.7	83.2	82.3	89.0	79.2	91.0	81.1	91.2	88.4	84.2	95.9	70.2	95.6	82.3	62.8	75.5	83.1
+SinPoint-MSF	85.8	83.1	80.1	87.3	79.1	91.1	77.4	91.1	88.1	85.1	95.6	72.8	95.4	81.8	60.7	75.8	83.4
DGCNN	84.8	82.2	75.1	81.3	78.2	90.6	73.6	90.8	87.8	84.4	95.6	57.8	92.8	80.6	51.5	73.9	82.8
+PointWOLF	85.2	82.9	73.3	83.5	76.7	90.8	76.7	91.4	89.2	85.2	95.8	53.7	94.0	80.1	54.9	74.3	83.4
+SinPoint-SSF	85.3	82.5	84.7	86.3	77.5	90.5	76.8	91.0	88.5	85.2	95.0	61.0	94.8	83.1	62.6	74.9	83.2
+SinPoint-MSF	85.5	83.1	86.3	87.0	78.9	90.7	74.3	91.2	87.8	85.9	95.5	62.6	94.6	82.0	61.3	74.0	83.1

Table 7: Complete part segmentation results (mIoU) on ShapeNetPart Yi et al. (2016).

Model	Base	+CDA	+PointMixup	+RSMix	+SageMix	+PointWOLF	+SinPoint(Ours)
PointNet++	84.8	85.1	85.5	85.4	85.7	85.2	85.8 (↑ 1.0)
DGCNN	84.8	85.0	85.3	85.2	85.4	85.2	85.5 (↑ 0.7)

5 CONCLUSION

We propose SinPoint, a novel data augmentation based a homeomorphism for Point Clouds that deforms point clouds by Sine functions while maintaining topological consistency. We only need to adjust the amplitude and frequency of the Sine function to generate a diverse and realistic sample with smoothly varying deformations, which brings significant improvements to point cloud tasks across several datasets. In the end, we conducted extensive experiments and demonstrated how SinPoint improves the performance of three representative networks on multiple datasets. Our findings show that the augmentations we produce are visually realistic and beneficial to the models, further validating the importance of our approach to understanding the local structure of point clouds.

REFERENCES

- 486
487
488 Iro Armeni, Ozan Sener, Amir R Zamir, Helen Jiang, Ioannis Brilakis, Martin Fischer, and Silvio
489 Savarese. 3d semantic parsing of large-scale indoor spaces. In *Proceedings of the IEEE conference*
490 *on computer vision and pattern recognition*, pp. 1534–1543, 2016.
- 491 Mark Anthony Armstrong. *Basic topology*. Springer Science & Business Media, 2013.
- 492
493 Jens Behley, Martin Garbade, Andres Milioto, Jan Quenzel, Sven Behnke, Cyrill Stachniss, and
494 Jurgen Gall. Semantickitti: A dataset for semantic scene understanding of lidar sequences. In
495 *Proceedings of the IEEE/CVF international conference on computer vision*, pp. 9297–9307, 2019.
- 496 Binjie Chen, Yunzhou Xia, Yu Zang, Cheng Wang, and Jonathan Li. Decoupled local aggregation
497 for point cloud learning. *arXiv preprint arXiv:2308.16532*, 2023.
- 498
499 Jingdao Chen, Zsolt Kira, and Yong K Cho. Deep learning approach to point cloud scene under-
500 standing for automated scan to 3d reconstruction. *Journal of Computing in Civil Engineering*, 33
501 (4):04019027, 2019a.
- 502 Xiaozhi Chen, Huimin Ma, Ji Wan, Bo Li, and Tian Xia. Multi-view 3d object detection network
503 for autonomous driving. In *Proceedings of the IEEE/CVF Conference on Computer Vision and*
504 *Pattern Recognition*, pp. 1907–1915, 2017.
- 505
506 Yunlu Chen, Vincent Tao Hu, Efstratios Gavves, Thomas Mensink, Pascal Mettes, Pengwan Yang,
507 and Cees GM Snoek. Pointmixup: Augmentation for point clouds. In *Computer Vision–ECCV*
508 *2020: 16th European Conference, Glasgow, UK, August 23–28, 2020, Proceedings, Part III 16*,
509 pp. 330–345. Springer, 2020.
- 510
511 Zhutian Chen, Wei Zeng, Zhiguang Yang, Lingyun Yu, Chi-Wing Fu, and Huamin Qu. LassoNet:
512 Deep lasso-selection of 3d point clouds. *IEEE Transactions on Visualization and Computer*
513 *Graphics*, pp. 195–204, 2019b.
- 514
515 Christopher Choy, JunYoung Gwak, and Silvio Savarese. 4d spatio-temporal convnets: Minkowski
516 convolutional neural networks. In *Proceedings of the IEEE/CVF conference on computer vision*
517 *and pattern recognition*, pp. 3075–3084, 2019.
- 518
519 WR Derrick. A condition under which a mapping is a homeomorphism. *The American Mathematical*
520 *Monthly*, 80(5):554–555, 1973.
- 521
522 Terrance DeVries and Graham W Taylor. Improved regularization of convolutional neural networks
523 with cutout. *arXiv preprint arXiv:1708.04552*, 2017.
- 524
525 Meng-Hao Guo, Jun-Xiong Cai, Zheng-Ning Liu, Tai-Jiang Mu, Ralph R Martin, and Shi-Min Hu.
526 Pct: Point cloud transformer. *Computational Visual Media*, 7:187–199, 2021.
- 527
528 Kaiming He, Xiangyu Zhang, Shaoqing Ren, and Jian Sun. Deep residual learning for image recog-
529 nition. In *Proceedings of the IEEE/CVF Conference on Computer Vision and Pattern Recognition*,
530 pp. 770–778, 2016.
- 531
532 Tao Hong, Zeren Zhang, and Jinwen Ma. Pcsalmix: Gradient saliency-based mix augmentation for
533 point cloud classification. In *IEEE International Conference on Acoustics, Speech and Signal*
534 *Processing*, pp. 1–5. IEEE, 2023.
- 535
536 Kiyosumi Kidono, Takeo Miyasaka, Akihiro Watanabe, Takashi Naito, and Jun Miura. Pedestrian
537 recognition using high-definition lidar. In *2011 IEEE Intelligent Vehicles Symposium (IV)*, pp.
538 405–410. IEEE, 2011.
- 539
540 Sihyeon Kim, Sanghyeok Lee, Dasol Hwang, Jaewon Lee, Seong Jae Hwang, and Hyunwoo J Kim.
541 Point cloud augmentation with weighted local transformations. In *Proceedings of the IEEE/CVF*
542 *international conference on computer vision*, pp. 548–557, 2021.
- 543
544 Dogyoon Lee, Jaeha Lee, Junhyeop Lee, Hyeongmin Lee, Minhyeok Lee, Sungmin Woo, and
545 Sangyoun Lee. Regularization strategy for point cloud via rigidly mixed sample. In *Proceedings*
546 *of the IEEE/CVF Conference on Computer Vision and Pattern Recognition*, pp. 15900–15909,
547 2021.

- 540 Sanghyeok Lee, Minkyu Jeon, Injae Kim, Yunyang Xiong, and Hyunwoo J Kim. Sagemix: Saliency-
541 guided mixup for point clouds. *Advances in Neural Information Processing Systems*, 35:23580–
542 23592, 2022.
- 543
544 Ruihui Li, Xianzhi Li, Pheng-Ann Heng, and Chi-Wing Fu. Pointaugmt: an auto-augmentation
545 framework for point cloud classification. In *Proceedings of the IEEE/CVF Conference on Com-
546 puter Vision and Pattern Recognition*, pp. 6378–6387, 2020.
- 547 Yangyan Li, Rui Bu, Mingchao Sun, Wei Wu, Xinhan Di, and Baoquan Chen. Pointcnn: Convolu-
548 tion on x-transformed points. *Advances in Neural Information Processing Systems*, 31, 2018.
- 549
550 Haojia Lin, Xiawu Zheng, Lijiang Li, Fei Chao, Shanshan Wang, Yan Wang, Yonghong Tian, and
551 Rongrong Ji. Meta architecture for point cloud analysis. In *Proceedings of the IEEE/CVF Con-
552 ference on Computer Vision and Pattern Recognition*, pp. 17682–17691, 2023.
- 553
554 Yiqun Lin, Zizheng Yan, Haibin Huang, Dong Du, Ligang Liu, Shuguang Cui, and Xiaoguang
555 Han. Fpconv: Learning local flattening for point convolution. In *Proceedings of the IEEE/CVF
556 Conference on Computer Vision and Pattern Recognition*, pp. 4293–4302, 2020a.
- 557
558 Zhi-Hao Lin, Sheng-Yu Huang, and Yu-Chiang Frank Wang. Convolution in the cloud: Learning
559 deformable kernels in 3d graph convolution networks for point cloud analysis. In *Proceedings of
560 the IEEE/CVF Conference on Computer Vision and Pattern Recognition*, pp. 1800–1809, 2020b.
- 561
562 Zhi-Hao Lin, Sheng-Yu Huang, and Yu-Chiang Frank Wang. Learning of 3d graph convolution net-
563 works for point cloud analysis. *IEEE Transactions on Pattern Analysis and Machine Intelligence*,
44(8):4212–4224, 2021.
- 564
565 Yongcheng Liu, Bin Fan, Shiming Xiang, and Chunhong Pan. Relation-shape convolutional neural
566 network for point cloud analysis. In *Proceedings of the IEEE/CVF Conference on Computer
567 Vision and Pattern Recognition*, pp. 8895–8904, 2019.
- 568
569 Ze Liu, Han Hu, Yue Cao, Zheng Zhang, and Xin Tong. A closer look at local aggregation operators
570 in point cloud analysis. In *Computer Vision–ECCV 2020: 16th European Conference, Glasgow,
571 UK, August 23–28, 2020, Proceedings, Part XXIII 16*, pp. 326–342. Springer, 2020.
- 572
573 Xu Ma, Can Qin, Haoxuan You, Haoxi Ran, and Yun Fu. Rethinking network design and local
574 geometry in point cloud: A simple residual mlp framework. *arXiv preprint arXiv:2202.07123*,
2022.
- 575
576 Luis E Navarro-Serment, Christoph Mertz, and Martial Hebert. Pedestrian detection and tracking
577 using three-dimensional lidar data. *The International Journal of Robotics Research*, 29(12):
1516–1528, 2010.
- 578
579 Jinyoung Park, Sanghyeok Lee, Sihyeon Kim, Yunyang Xiong, and Hyunwoo J Kim. Self-
580 positioning point-based transformer for point cloud understanding. In *Proceedings of the
581 IEEE/CVF Conference on Computer Vision and Pattern Recognition*, pp. 21814–21823, 2023.
- 582
583 Charles R Qi, Hao Su, Kaichun Mo, and Leonidas J Guibas. Pointnet: Deep learning on point sets
584 for 3d classification and segmentation. In *Proceedings of the IEEE/CVF Conference on Computer
585 Vision and Pattern Recognition*, pp. 652–660, 2017a.
- 586
587 Charles R Qi, Wei Liu, Chenxia Wu, Hao Su, and Leonidas J Guibas. Frustum pointnets for 3d
588 object detection from rgb-d data. In *Proceedings of the IEEE/CVF Conference on Computer
589 Vision and Pattern Recognition*, pp. 918–927, 2018.
- 590
591 Charles Ruizhongtai Qi, Li Yi, Hao Su, and Leonidas J Guibas. Pointnet++: Deep hierarchical
592 feature learning on point sets in a metric space. *Advances in Neural Information Processing
593 Systems*, 30, 2017b.
- 594
595 Xiaojuan Qi, Renjie Liao, Jiaya Jia, Sanja Fidler, and Raquel Urtasun. 3d graph neural networks for
596 rgbd semantic segmentation. In *Proceedings of the IEEE International Conference on Computer
597 Vision*, pp. 5199–5208, 2017c.

- 594 Guocheng Qian, Yuchen Li, Houwen Peng, Jinjie Mai, Hasan Hammoud, Mohamed Elhoseiny, and
595 Bernard Ghanem. Pointnext: Revisiting pointnet++ with improved training and scaling strategies.
596 *Advances in Neural Information Processing Systems*, 35:23192–23204, 2022.
597
- 598 Jiawei Ren, Liang Pan, and Ziwei Liu. Benchmarking and analyzing point cloud classification under
599 corruptions. In *International Conference on Machine Learning*, pp. 18559–18575. PMLR, 2022.
600
- 601 Radu Bogdan Rusu, Zoltan Csaba Marton, Nico Blodow, Mihai Dolha, and Michael Beetz. To-
602 wards 3d point cloud based object maps for household environments. *Robotics and Autonomous
603 Systems*, 56(11):927–941, 2008.
- 604 Yiru Shen, Chen Feng, Yaoqing Yang, and Dong Tian. Mining point cloud local structures by kernel
605 correlation and graph pooling. In *Proceedings of the IEEE/CVF Conference on Computer Vision
606 and Pattern Recognition*, pp. 4548–4557, 2018.
607
- 608 Martin Simonovsky and Nikos Komodakis. Dynamic edge-conditioned filters in convolutional neu-
609 ral networks on graphs. In *Proceedings of the IEEE/CVF Conference on Computer Vision and
610 Pattern Recognition*, pp. 3693–3702, 2017.
- 611 Daisuke Sugimura, Tomoaki Yamazaki, and Takayuki Hamamoto. Three-dimensional point cloud
612 object detection using scene appearance consistency among multi-view projection directions.
613 *IEEE Transactions on Circuits and Systems for Video Technology*, 30(10):3345–3357, 2020. doi:
614 10.1109/TCSVT.2019.2957821.
- 615 Bilal Taha, Munawar Hayat, Stefano Berretti, Dimitrios Hatzinakos, and Naoufel Werghi. Learned
616 3d shape representations using fused geometrically augmented images: Application to facial ex-
617 pression and action unit detection. *IEEE Transactions on Circuits and Systems for Video Technol-
618 ogy*, 30(9):2900–2916, 2020. doi: 10.1109/TCSVT.2020.2984241.
619
- 620 Hugues Thomas, Charles R Qi, Jean-Emmanuel Deschaud, Beatriz Marcotegui, François Goulette,
621 and Leonidas J Guibas. Kpconv: Flexible and deformable convolution for point clouds. In
622 *Proceedings of the IEEE/CVF international conference on computer vision*, pp. 6411–6420, 2019.
623
- 624 Mikaela Angelina Uy, Quang-Hieu Pham, Binh-Son Hua, Thanh Nguyen, and Sai-Kit Yeung. Revis-
625 iting point cloud classification: A new benchmark dataset and classification model on real-world
626 data. In *Proceedings of the IEEE/CVF international conference on computer vision*, pp. 1588–
627 1597, 2019.
- 628 Francesco Verdoja, Diego Thomas, and Akihiro Sugimoto. Fast 3d point cloud segmentation using
629 supervoxels with geometry and color for 3d scene understanding. In *2017 IEEE International
630 Conference on Multimedia and Expo (ICME)*, pp. 1285–1290. IEEE, 2017.
631
- 632 Vikas Verma, Alex Lamb, Christopher Beckham, Amir Najafi, Ioannis Mitliagkas, David Lopez-
633 Paz, and Yoshua Bengio. Manifold mixup: Better representations by interpolating hidden states.
634 In *International conference on machine learning*, pp. 6438–6447. PMLR, 2019.
- 635 Lei Wang, Yuchun Huang, Yaolin Hou, Shenman Zhang, and Jie Shan. Graph attention convolution
636 for point cloud semantic segmentation. In *Proceedings of the IEEE/CVF Conference on Computer
637 Vision and Pattern Recognition*, pp. 10296–10305, 2019a.
638
- 639 Yi Wang, Jiase Wang, Jinpeng Li, Zixu Zhao, Guangyong Chen, Anfeng Liu, and Pheng Ann Heng.
640 Pointpatchmix: Point cloud mixing with patch scoring. In *Proceedings of the AAAI Conference
641 on Artificial Intelligence*, volume 38, pp. 5686–5694, 2024.
- 642 Yue Wang, Yongbin Sun, Ziwei Liu, Sanjay E Sarma, Michael M Bronstein, and Justin M Solomon.
643 Dynamic graph cnn for learning on point clouds. *ACM Transactions on Graphics (tog)*, 38(5):
644 1–12, 2019b.
645
- 646 Wenxuan Wu, Zhongang Qi, and Li Fuxin. Pointconv: Deep convolutional networks on 3d point
647 clouds. In *Proceedings of the IEEE/CVF Conference on Computer Vision and Pattern Recogni-
tion*, pp. 9621–9630, 2019.

- 648 Zhirong Wu, Shuran Song, Aditya Khosla, Fisher Yu, Linguang Zhang, Xiaoou Tang, and Jianx-
649 iong Xiao. 3d shapenets: A deep representation for volumetric shapes. In *Proceedings of the*
650 *IEEE/CVF Conference on Computer Vision and Pattern Recognition*, pp. 1912–1920, 2015.
- 651
- 652 Tiange Xiang, Chaoyi Zhang, Yang Song, Jianhui Yu, and Weidong Cai. Walk in the cloud: Learning
653 curves for point clouds shape analysis. In *Proceedings of the IEEE/CVF International Conference*
654 *on Computer Vision*, pp. 915–924, 2021.
- 655 Mingye Xu, Zhipeng Zhou, Junhao Zhang, and Yu Qiao. Investigate indistinguishable points in
656 semantic segmentation of 3d point cloud. In *Proceedings of the AAAI Conference on Artificial*
657 *Intelligence*, pp. 3047–3055, 2021a.
- 658 Mutian Xu, Runyu Ding, Hengshuang Zhao, and Xiaojuan Qi. Paconv: Position adaptive con-
659 volution with dynamic kernel assembling on point clouds. In *Proceedings of the IEEE/CVF*
660 *Conference on Computer Vision and Pattern Recognition*, pp. 3173–3182, 2021b.
- 661
- 662 Mutian Xu, Junhao Zhang, Zhipeng Zhou, Mingye Xu, Xiaojuan Qi, and Yu Qiao. Learning
663 geometry-disentangled representation for complementary understanding of 3d object point cloud.
664 In *Proceedings of the AAAI Conference on Artificial Intelligence*, pp. 3056–3064, 2021c.
- 665 Lingfeng Yang, Xiang Li, Borui Zhao, Renjie Song, and Jian Yang. Recursivemix: Mixed learning
666 with history. *Advances in Neural Information Processing Systems*, 35:8427–8440, 2022.
- 667
- 668 Li Yi, Vladimir G Kim, Duygu Ceylan, I-Chao Shen, Mengyan Yan, Hao Su, Cewu Lu, Qixing
669 Huang, Alla Sheffer, and Leonidas Guibas. A scalable active framework for region annotation in
670 3d shape collections. *ACM Transactions on Graphics (ToG)*, 35(6):1–12, 2016.
- 671 Sangdoon Yun, Dongyoon Han, Seong Joon Oh, Sanghyuk Chun, Junsuk Choe, and Youngjoon Yoo.
672 Cutmix: Regularization strategy to train strong classifiers with localizable features. In *Proceed-*
673 *ings of the IEEE/CVF international conference on computer vision*, pp. 6023–6032, 2019.
- 674
- 675 Hongyi Zhang, Moustapha Cisse, Yann N Dauphin, and David Lopez-Paz. mixup: Beyond empirical
676 risk minimization. *arXiv preprint arXiv:1710.09412*, 2017.
- 677 Jinlai Zhang, Lyujie Chen, Bo Ouyang, Binbin Liu, Jihong Zhu, Yujin Chen, Yanmei Meng, and
678 Danfeng Wu. Pointcutmix: Regularization strategy for point cloud classification. *Neurocomput-*
679 *ing*, 505:58–67, 2022.
- 680
- 681 Renrui Zhang, Lihui Wang, Yali Wang, Peng Gao, Hongsheng Li, and Jianbo Shi. Parameter is not
682 all you need: Starting from non-parametric networks for 3d point cloud analysis. *arXiv preprint*
683 *arXiv:2303.08134*, 2023.
- 684 Lichen Zhao, Jinyang Guo, Dong Xu, and Lu Sheng. Transformer3d-det: Improving 3d object
685 detection by vote refinement. *IEEE Transactions on Circuits and Systems for Video Technology*,
686 31(12):4735–4746, 2021. doi: 10.1109/TCSVT.2021.3102025.
- 687
- 688 Zhun Zhong, Liang Zheng, Guoliang Kang, Shaozi Li, and Yi Yang. Random erasing data aug-
689 mentation. In *Proceedings of the AAAI Conference on Artificial Intelligence*, pp. 13001–13008,
690 2020.
- 691
- 692
- 693
- 694
- 695
- 696
- 697
- 698
- 699
- 700
- 701

702 A APPENDIX

703
704
705 In this Appendix, we provide detailed discussions and experimental results. They include: 1) Imple-
706 mentation details of SinPoint, 2) Proof of Theorem 1: a homeomorphism Based on Sine Function;
707 and 3) Additional ablation studies and analyses.

708 B A IMPLEMENTATION DETAIL

709
710
711 We conduct experiments using Python and PyTorch with two NVIDIA TITAN RTX for point clouds.
712 Following the original configuration in Qi et al. (2017a;b); Wang et al. (2019b), we use the SGD
713 optimizer with an initial learning rate of 10^{-1} and weight decay of 10^{-3} for PointNet Qi et al.
714 (2017a) and PointNet++ Qi et al. (2017b) and SGD with an initial learning rate of 10^{-2} and weight
715 decay of 10^{-4} for DGCNN Wang et al. (2019b). We train models with a batch size of 32 for 300
716 epochs. For a fair comparison with previous works Chen et al. (2020); Zhang et al. (2022), we also
717 adopt conventional data augmentations with our framework (i.e., scaling and shifting for MN40 Wu
718 et al. (2015) and rotation and jittering for ScanObjectNN Uy et al. (2019)). For hyperparameters of
719 SinPoint-SSF and SinPoint-MSF, we opt $A = 0.6, w = 2.5, k = 4$ in the entire experiment.
720

721 C PROOF

722
723 **Theorem 1. (Homeomorphism Based on Sine Function)** Given two topological spaces X, Y , and
724 given a mapping $f : X \rightarrow Y = X + A\sin(\omega X + \varphi)$, if $-1 \leq A\omega \leq 1$, then f is a homeomorphism,
725 else f is a local homeomorphism.
726

727 **1) Proof: if $-1 \leq A\omega \leq 1$, then f is a homeomorphism**

728 Step 1: *Continuous*

729
730 Let $g(x) = x, h(x) = A\sin(\omega x + \varphi), x \in R$. Since $g(x) = x$ is a continuous function and
731 $h(x) = A\sin(\omega x + \varphi)$ is also a continuous function, then $f(x) = g(x) + h(x) = x + A\sin(\omega x + \varphi)$
732 must be a continuous function.
733

734 Step 2: *Bijjective*

735 Let $f(x) = x + A\sin(\omega x + \varphi), x \in R$. Then $f'(x) = 1 + A\omega\cos(\omega x + \varphi), x \in R$.

736 Since $A\omega\cos(\omega x + \varphi) \in [-A\omega, A\omega]$. Next $f'(x) \in [1 - A\omega, 1 + A\omega]$.

737 Let $f'(x) > 0 \Rightarrow 1 + A\omega\cos(\omega x + \varphi) > 0 \Rightarrow 1 - A\omega > 0 \Rightarrow A\omega < 1$.

738 Let $f'(x) < 0 \Rightarrow 1 + A\omega\cos(\omega x + \varphi) < 0 \Rightarrow 1 + A\omega < 0 \Rightarrow A\omega > -1$.

739 As $-1 \leq A\omega \leq 1, f$ is a monotone function. In this case, $\forall A\omega \in [-1, 1], \exists f^{-1}$ is f

740 In this case, $\forall A\omega \in [-1, 1], f$ must be invertible, and the inverse function of f is f^{-1} .

741 Thus, f is bijective if and only if $-1 \leq A\omega \leq 1$.

742 Finally, when $-1 \leq A\omega \leq 1$, then $f : X \rightarrow Y = X + A\sin(\omega X + \varphi)$ is a homeomorphism.

743 **2) Proof: if $A\omega \in R$, then f is a local homeomorphism**

744 as we know, $h(x) = A\sin(\omega x + \varphi), x \in R$ is a periodic function. where $T = \frac{2k\pi}{\omega}$.

745 Let $2k\pi - \frac{pi}{2} \leq \omega x + \varphi \leq 2k\pi + \frac{pi}{2}, k \in Z$, then $\frac{2k\pi - \frac{pi}{2} - \varphi}{\omega} \leq x \leq \frac{2k\pi + \frac{pi}{2} - \varphi}{\omega}$, now f is strictly
746 increasing.

747 Let $2k\pi + \frac{pi}{2} \leq \omega x + \varphi \leq 2k\pi + \frac{3pi}{2}, k \in Z$, then $\frac{2k\pi + \frac{pi}{2} - \varphi}{\omega} \leq x \leq \frac{2k\pi + \frac{3pi}{2} - \varphi}{\omega}$, now f is strictly
748 decreasing.

749 Thus, when $A\omega \in R, \forall u \in R, \exists U$ such that f_U is monotone and f is a local homeomorphism.
750
751
752
753
754
755

D ANALYSIS

D.1 DETAILED ANALYSIS OF HOW OUR METHOD AFFECTS PART BOUNDARIES

As **Sard's Theorem** stated, when the mapping is smooth and under the condition of general position, the set of points with zero Jacobian determinant will have the property of measure zero, but in practice, the frequently changing sign of the determinant may still lead to the folding phenomenon. Below we carefully analyze how our method affects part boundaries.

Given the mapping $P' = P + A \sin(\omega P + \phi)$, we can see it as a transformation from P to P' , where $P = (x, y, z)$ and $P' = (x', y', z')$ denote points in 3D space.

Calculate the Jacobian.

Set:

$$g(P) = A \sin(\omega P + \phi). \quad (6)$$

So the transformation can be written as follows:

$$P' = P + g(P). \quad (7)$$

To calculate the Jacobian $J_{P'}(P)$ of this transformation, we need to take the derivatives with respect to the components of P' with respect to P separately.

1 Write the component forms of P' Suppose each component form is as follows:

$$x' = x + A_x \sin(\omega_x x + \phi_x). \quad (8)$$

$$y' = y + A_y \sin(\omega_y y + \phi_y). \quad (9)$$

$$z' = z + A_z \sin(\omega_z z + \phi_z). \quad (10)$$

Thus, $P' = (x', y', z')$ is obtained by adding $P = (x, y, z)$ to the sine transform of the components.

2 Calculate the elements of the Jacobian matrix.

The Jacobian matrix $J_{P'}(P)$ is of the form:

$$J_{P'}(P) = \begin{bmatrix} \frac{\partial x'}{\partial x} & \frac{\partial x'}{\partial y} & \frac{\partial x'}{\partial z} \\ \frac{\partial y'}{\partial x} & \frac{\partial y'}{\partial y} & \frac{\partial y'}{\partial z} \\ \frac{\partial z'}{\partial x} & \frac{\partial z'}{\partial y} & \frac{\partial z'}{\partial z} \end{bmatrix} \quad (11)$$

Since x' depends only on x , y' depends only on y , and z' depends only on z , the partial derivative matrix is a diagonal matrix.

Diagonal elements are computed:

1) For $\frac{\partial x'}{\partial x}$:

$$\frac{\partial x'}{\partial x} = 1 + A_x \omega_x \cos(\omega_x x + \phi_x) \quad (12)$$

2) For $\frac{\partial y'}{\partial y}$:

$$\frac{\partial y'}{\partial y} = 1 + A_y \omega_y \cos(\omega_y y + \phi_y) \quad (13)$$

3) For $\frac{\partial z'}{\partial z}$:

$$\frac{\partial z'}{\partial z} = 1 + A_z \omega_z \cos(\omega_z z + \phi_z) \quad (14)$$

So the Jacobian matrix is as follows:

$$J_{P'}(P) = \begin{bmatrix} 1 + A_x \omega_x \cos(\omega_x x + \phi_x) & 0 & 0 \\ 0 & 1 + A_y \omega_y \cos(\omega_y y + \phi_y) & 0 \\ 0 & 0 & 1 + A_z \omega_z \cos(\omega_z z + \phi_z) \end{bmatrix} \quad (15)$$

The determinant of this Jacobian is:

$$\det(J_{P'}(P)) = (1 + A_x \omega_x \cos(\omega_x x + \phi_x)) \cdot (1 + A_y \omega_y \cos(\omega_y y + \phi_y)) \cdot (1 + A_z \omega_z \cos(\omega_z z + \phi_z)). \quad (16)$$

According to **Sard's Theorem**:

If $\det(J_{P'}(P)) > 0$, the map is orientation-preserving near that point, that is, no direction flip occurs locally.

If $\det(J_{P'}(P)) < 0$, the map is orientation-reversing near that point, that is, the local direction has been flipped.

Thus:

When $|Aw| < 1$, $\det(J_{P'}(P)) > 0$, not affect the part boundaries.

When $|Aw| > 1$, that is, $|A|$ and $|w|$ are large and in the same direction, the determinant may change sign in different regions, which means that the mapping may alternately hold or flip directions in different regions. At this time, the determinant of some regions approaches zero or becomes negative, which may cause the points in local regions to be compressed or collapsed, affecting the part boundaries. In addition, the degree of specific influence on the boundary is also affected by the parameter. When the parameter value does not change much, this influence can be ignored.

As shown in Figure 6, selecting too large a parameter can result in folding, which may affect **part boundaries**. Therefore, in order to ensure topological consistency and no drastic folding occurs, we choose an appropriate A and w . As in the ablation experiments in Tables 9 and 10, we finally choose $w = 2.5$ and $A = 0.6$. The model achieves better performance at this time, which means that slight folding is beneficial to the model. However, the above situation does not affect **label consistency**.

D.2 DETAILED ANALYSIS OF LABEL CONSISTENCY

1) One-to-one mapping between point clouds and labels.

Given point cloud $P = (p_1, p_2, \dots, p_n)$. Each point p_i has a corresponding label l_i . So you can get a one-to-one correspondence:

$$p_1 \rightarrow l_1, p_2 \rightarrow l_2, \dots, p_n \rightarrow l_n. \quad (17)$$

This means that for each point p_i , it has a corresponding label l_i , which is associated with the geometric position of the point.

2) Definition of homeomorphic mapping.

A homeomorphic map $f(x)$ is a map that preserves topology and changes the positions of points but not the relative relations between them.

If we deform the point cloud by the homeomorphic mapping $f(P)$, then the new point cloud P' is:

$$P' = P + f(P). \quad (18)$$

Therefore, each point position of the new point cloud P' is $p'_i = p_i + f(p_i)$, that is, each point p_i moves to the new position p'_i by mapping $f(x)$.

3) Label consistency.

Since the homeomorphic mapping one-to-one correspondence of points in the point cloud, the index and label of each point are kept consistent after the point cloud is deformed. In other words, the label l_i corresponding to the deformed position p'_i does not change. We can obtain the following relationship:

$$p'_1 \rightarrow p_1 \rightarrow l_1, p'_2 \rightarrow p_2 \rightarrow l_2, \dots, p'_n \rightarrow p_n \rightarrow l_n. \quad (19)$$

Thus:

$$p'_1 \rightarrow l_1, p'_2 \rightarrow l_2, \dots, p'_n \rightarrow l_n. \quad (20)$$

This means that in the deformed point cloud P' , the label of each point p'_i remains the same as the label of p_i in the original point cloud P .

E ADDITIONAL EXPERIMENTS

E.1 MEAN AND STANDARD DEVIATION

Performance oscillation is an essential issue in point cloud benchmarks. However, for a fair comparison with the numbers reported in PointMixup Chen et al. (2020) RSMix Lee et al. (2021), and SageMix Lee et al. (2022), we followed the prevalent evaluation metric in point clouds, which reports the best validation accuracy. Apart from this, to make the experiment fair, like SageMix, we provide the additional results with five runs on OBJ_ONLY Uy et al. (2019) and report the mean and variance of our method, and the experimental results are shown in Table 8.

Table 8: Mean and standard deviation measures on OBJ_ONLY

Method	Model		
	PointNet	PointNet++	DGCNN
Base	78.56±0.51	86.14±0.39	85.72±0.44
+PointMixup	78.88±0.28	87.50±0.26	86.26±0.34
+RSMix	77.60±0.56	87.30±0.65	85.88±0.59
+SageMix	79.14±0.30	88.42±0.26	87.32±0.53
+SinPoint(Ours)	82.21±0.36	89.83±0.35	88.64±0.55

E.2 ABLATION STUDIES AND ANALYSES

Ablation study of angular velocity ω . We also share the quantitative analysis of the ω with DGCNN and OBJ_ONLY in Table 9. We observed that SinPoint, with a wide range of ω (2.5 to 4.5), consistently outperforms PointWOLF 88.8%. At the same time, all cases exceeded the base 86.2%. This shows that the network can learn more representative features after deformation.

Table 9: Ablation study of angular velocity ω .

w	0.5	1.0	1.5	2.0	2.5	3.0	3.5	4.0	4.5	5.0	7.5	10.0
Rnad	88.468	88.812	88.640	88.985	90.189	89.329	89.329	88.985	88.985	88.640	89.296	88.124
Fixed	87.673	86.403	86.747	85.714	85.714	86.747	86.403	86.231	86.919	87.091	86.059	86.059

Ablation study of amplitude A . The amplitude A of the Sine function controls the degree of deformation in SinPoint. As shown in Table 10, the larger the A , the larger the deformation. However, as shown in Figure 6, too large deformation will lead to the loss of local geometric information. Therefore, we need proper deformation.

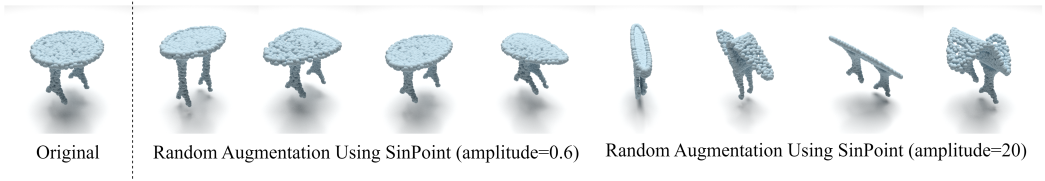


Figure 6: Visualization of ablation results for different parameters of SinPoint.

Ablation study of anchor points k in SinPoint-MSF. As can be seen from Table 11, when anchor points $k = 4$, the performance reaches 89.845%, but in SinPoint-SSF, the classification performance can reach 90.189%. Although the SinPoint-MSF is effective, exceeding the baseline by 3.6%, the SinPoint-SSF is the best in the classification task. We further verify the performance difference between SinPoint-SSF and SinPoint-MSF in the classification experiment, as shown in Table 12, and we find that SSF performs better.

Ablation study of amplitude (A) and angular velocity ω sampling. We explore the effectiveness of amplitude A and angular velocity ω sampling. Table 13 shows the results with various sampling

918
919
920
921
922
923
924
925
926
927
928
929
930
931Table 10: Ablation study of amplitude A .

A	0.2	0.4	0.6	0.8	1.0
OA (%)	88.985	88.812	90.189	89.329	88.985
mAcc (%)	87.811	87.663	89.045	88.642	88.303

Table 11: Ablation study of anchor points k in SinPoint-MSF.

k	1	2	3	4	5	6
RPS	88.985	89.535	89.315	89.845	88.468	89.329
FPS	88.812	88.985	88.812	89.329	88.315	88.985

methods for amplitude A and angular velocity ω . Uniform and Gaussian sampling introduce +3.9% and 2.8% gains over base DGCNN. The OA with Uniform sampling is 2.1% higher than Gaussian sampling, which means that uniform sampling leads to greater diversity and maximizes model performance.

3D part segmentation performance under Various Baselines. The effectiveness of SinPoint is further validated across a variety of network architectures in ShapeNetPart Yi et al. (2016), including PointNet Qi et al. (2017a), PointNet++ Qi et al. (2017b), DGCNN Wang et al. (2019b), CurveNet Xiang et al. (2021), 3DGCN Lin et al. (2021), GDANet Xu et al. (2021c), PointMLP Ma et al. (2022), SPoTr Park et al. (2023), PointMetaBase Lin et al. (2023) and DeLA Chen et al. (2023). Table 14 shows that SinPoint has a consistent improvement of mean Inter-over-Union (mIoU) over the baselines (+0.1~1.0%).

Performance on scene segmentation. We added additional experiments to the S3DIS Armeni et al. (2016) and SemanticKITTI Behley et al. (2019) datasets. As shown in Table 15, our SinPoint is still able to improve MinkNet Choy et al. (2019) performance.

E.3 VISUALIZATION

Convergence analysis. As shown in Figure 7, our SinPoint demonstrates faster convergence during the training phase and achieves higher accuracy than the baseline. Consistent performance improvement is achieved under various parameter Settings.

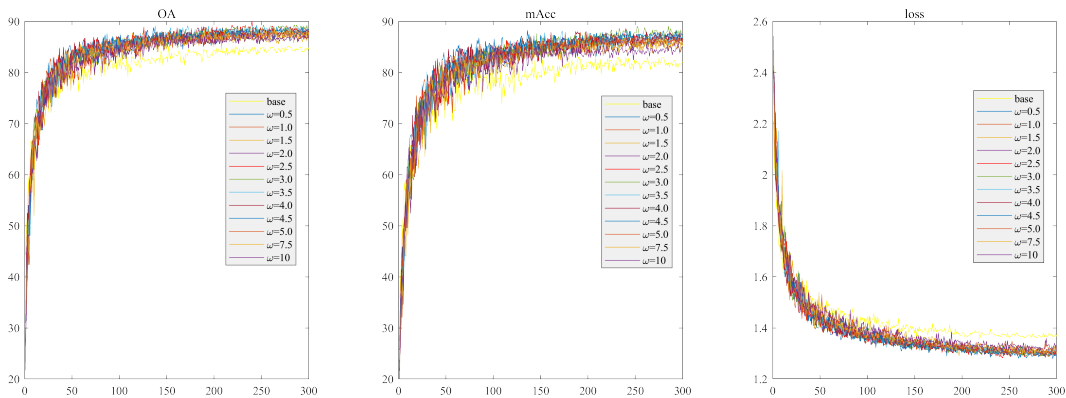


Figure 7: Convergence curve during the model training phase. Our SinPoint has a faster convergence speed and higher convergence accuracy than the baseline.

965
966
967
968
969
970
971

Training efficiency. As shown in Table 16, Our SinPoint achieves the best performance while reducing the time per training epoch. Notably, the training time is reduced by 10 times compared to PointAugment, 6 times compared to SageMix, and 2 times compared to PointWOLF.

972
973
974
975
976
977
978
979
980
981
982
983
984
985
986
987
988
989
990
991
992
993
994
995
996
997
998
999
1000
1001
1002
1003
1004
1005
1006
1007
1008
1009
1010
1011
1012
1013
1014
1015
1016
1017
1018
1019
1020
1021
1022
1023
1024
1025

Table 12: Ablation study of SinPoint-SSF and SinPoint-MSF on ScanObjectNN.

Method	SinPoint-SSF	SinPoint-MSF
OA	89.845	90.189

Table 13: Ablation study on amplitude A and angular velocity ω sampling.

	OA	mAcc
base	85.829±0.296	83.375±0.395
Uniform	89.759±0.431	88.636±0.445
Gaussian	87.607±0.344	85.494±0.409

Qualitative results of SinPoint. In Figure 8, we give a visualization of more augmented samples. In Figure 9, we present an augmented sample visualization comparison between SinPoint-SSF and SinPoint-MSF.

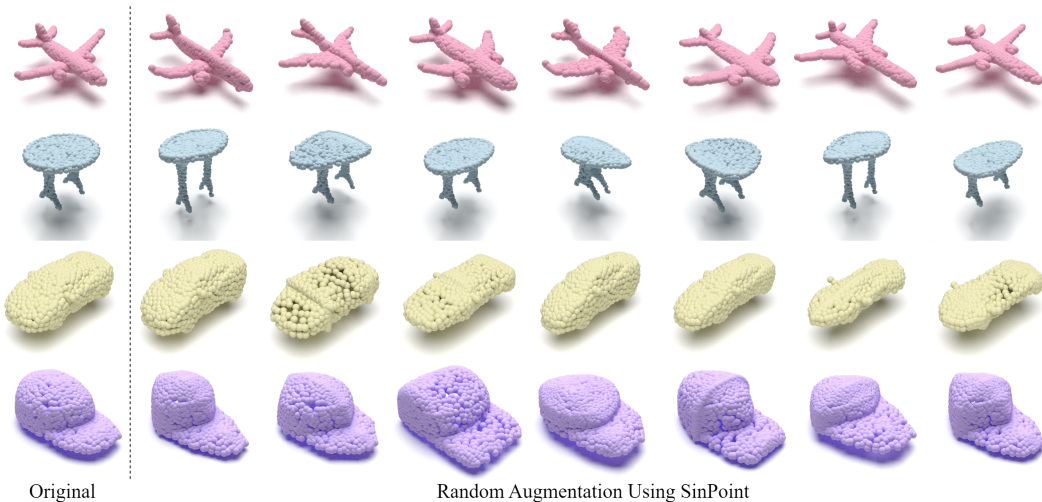


Figure 8: Augmented point clouds using SinPoint. In each row, the left-most sample is the original, and the remaining samples are its transformed results.

Qualitative results compare SinPoint with PointWOLF. We compare our SinPoint with PointWOLF in geometric diversity and topological consistency of point clouds. As can be seen from Figure 10, our SinPoint is entirely superior to PointWOLF and does not require **AugTune** Kim et al. (2021). The results generated by our SinPoint are more in line with the real world. On the contrary, many of the results generated by PointWOLF are out of the reality.

E.4 DISCUSSION AND FUTURE WORK

In the future, we will apply SinPoint to more tasks, such as feature space augmentation, few-shot learning Liu et al. (2019); Qi et al. (2017a), semantic segmentation Chen et al. (2019b); Xu et al. (2021a); Wang et al. (2019a), object detection Taha et al. (2020); Zhao et al. (2021); Sugimura et al. (2020), etc. It is worth noting, however, that different tasks require different considerations. For example, in few-shot learning, SinPoint maximizes the diversity of training data when samples are extremely scarce. For object detection, SinPoint can generate richer 3D transformations for various object instances in a 3D scene, and so on. Therefore, SinPoint will be easily extended to other tasks.

Table 14: **Part segmentation performance in various architectures on ShapeNetPart Yi et al. (2016). The proposed SinPoint shows consistent improvements over baselines.**

Model	PointNet	PointNet++	DGCNN	CurveNet	3DGCN	GDANet	PointMLP	SPoTr	PointMetaBase	DeLA
Base	83.5	84.8	84.8	86.6	86.4	86.1	85.8	87.0	86.9	87.0
+SinPoint	84.4 (↑ 0.9)	85.8 (↑ 1.0)	85.5 (↑ 0.7)	86.8 (↑ 0.2)	86.6 (↑ 0.2)	86.2 (↑ 0.1)	86.1 (↑ 0.3)	87.2 (↑ 0.2)	87.3 (↑ 0.4)	87.4 (↑ 0.4)

Table 15: **SinPoint on S3DIS and SemanticKITTI.**

Method	S3DIS (mIoU)	SemanticKITTI (mIoU)
MinkNet	64.8	55.9
+SinPoint (Ours)	65.4(+0.6)	63.5(+7.6)

F COMPARE TO OTHER METHODS

F.1 CONVENTIONAL DATA AUGMENTATION

A Conventional Data Augmentation (CDA) Qi et al. (2017a;b); Wang et al. (2019b) for point clouds applies a global similarity transformation (e.g., scaling, rotation, and translation) and point-wise jittering. Given a set of points $P = \{p_i | i = 1, 2, \dots, N\}$, where N represents the number of points in the Euclidean space (x, y, z) . The augmented point cloud P' is given as follows:

$$P' = SRP + B. \quad (21)$$

where $S > 0$ is a scaling factor, R is a 3D rotation matrix, and $B \in R^{N \times 3}$ is a translation matrix with global translation and point-wise jittering. Typically, R is an extrinsic rotation parameterized by a uniformly drawn Euler angle for the up-axis orientation. Scaling and translation factors are uniformly drawn from an interval, and point-wise jittering vectors are sampled from a truncated Gaussian distribution.

Obviously, when B does not exist, CDA is a rigid transformation, and when B exists, CDA is simply a similarity transformation with jitter. Thus, CDA cannot simulate diverse shapes and deformable objects, and the enhanced sample has poor diversity.

F.2 MIX-AUGMENTATION

Several works Chen et al. (2020); Lee et al. (2021) tried to leverage the Mixup in point cloud. PointMixup linearly interpolates two point clouds by

$$P' = \{\lambda p_i^\alpha + (1 - \lambda)p_{\phi^*(i)}^\beta\}_i^n, y' = \lambda y^\alpha + (1 - \lambda)y^\beta. \quad (22)$$

$$\phi^* = \arg \min_{\phi \in \Phi} \sum_{i=1}^n \|p_i^\alpha + p_{\phi(i)}^\beta\|_2 \quad (23)$$

where $P^t = \{p_1^t, \dots, p_n^t\}$ is the set of points with $t \in \{\alpha, \beta\}$, n is the number of points, and $\phi^* : \{1, \dots, n\} \rightarrow \{1, \dots, n\}$ is the optimal bijective assignment between two point clouds. In RSMix Lee et al. (2021), they generate an augmented sample by merging the subsets of two objects, defined as $P' = (P^\alpha - S^\alpha) \cup S^{\beta \rightarrow \alpha}$, where $S^t \subset P^t$ t is the rigid subset and $S^{\beta \rightarrow \alpha}$ denotes S^β translated to the center of S^α . SageMix sequentially selects the query point based on the saliency scores to improve the above method.

Table 16: Comparisons of the training efficiency on ModelNet40 using PointNet.

Method	PointAugment	SageMix	PointWOLF	SinPoint (Ours)
OA (%)	74.4	79.5	78.7	82.6
Time (sec)	84	51	15	8



1087
1088
1089
1090
1091
1092
1093
1094
1095
1096
1097
1098
1099
1100
1101
1102
1103
1104
1105
1106
1107
1108
1109
1110
1111
1112
1113
1114
1115
1116
1117
1118
1119
1120
1121
1122
1123
1124
1125
1126
1127
1128
1129
1130
1131
1132
1133

Figure 9: Visualization comparison of our SinPoint. The left is SinPoint-SSF, right is SinPoint-MSF. SinPoint-MSF can produce varying degrees of local deformation in different regions.

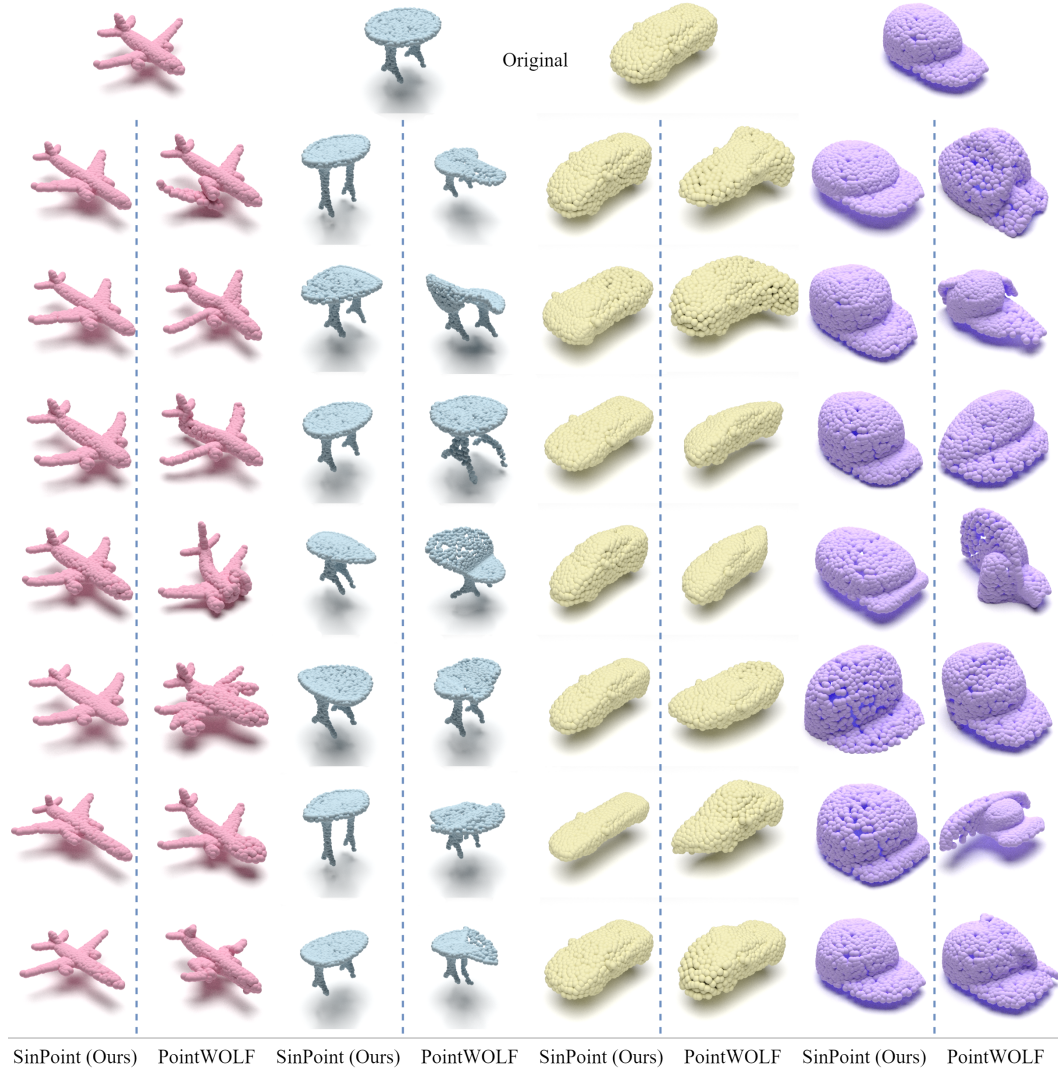


Figure 10: Visualization comparison of our SinPoint with PointWOLF. The top original point cloud, each shape left is SinPoint, right is PointWOLF. The samples generated by our SinPoint are more diverse and realistic.

Although these methods have shown that Mixup is effective for point clouds, some limitations have remained unresolved: loss of original structures, discontinuity at the boundary, and loss of discriminative regions. Therefore, although the method based on mixup can increase the diversity of samples by mixup different samples, it destroys the point cloud structure.

1134 F.3 SELF-AUGMENTATION
1135

1136 A representative method is PointWOLF. PointWOLF generates deformation for point clouds by a
 1137 convex combination of multiple transformations with smoothly varying weights. PointWOLF first
 1138 selects several anchor points and locates random local transformations (e.g., similarity transforma-
 1139 tions) at the anchor points. Based on the distance from a point in the input to the anchor points,
 1140 PointWOLF differentially applies the local transformations. The smoothly varying weights based
 1141 on the distance to the anchor points allow spatially continuous augmentation and generate realistic
 1142 samples. Given an anchor point $p_j^A \in P^A$, the local transformation for an input point $p_i^A \in P_i$ can
 1143 be written as:

$$1144 p_i^j = S_j R_j (p_i - p_j^A) + B_j + p_j^A. \quad (24)$$

1145 where R_j , S_j and B_j are rotation matrix, scaling matrix and translation vector b_j respectively
 1146 which specifically correspond to p_j^A . S is a diagonal matrix with three positive real values, i.e.,
 1147 $S = \text{diag}(s_x, s_y, s_z)$ to allow different scaling factors for different axes.

1148 Due to the local rotation and translation, the local separation from the main body will cause the
 1149 topological structure of the point cloud to change, so PointWOLF is not a homeomorphism and
 1150 cannot guarantee the topological consistency.

1151 Meanwhile, AugTune is also required due to the poor performance of the PointWOLF direct trans-
 1152 form. For N points and M anchor points, the time complexity of PointWOLF is $O(MN) + O(N)$.
 1153 However, our SinPoint can produce realistic augmented data without interpolation, and our SinPoint
 1154 time complexity is only $O(N)/O(MN)$, which can reduce the amount of computation.

1155
1156
1157
1158
1159
1160
1161
1162
1163
1164
1165
1166
1167
1168
1169
1170
1171
1172
1173
1174
1175
1176
1177
1178
1179
1180
1181
1182
1183
1184
1185
1186
1187